Int. J. Solids Structures Vol. 23, No. 6, pp. 669–692, 1987
Printed in Great Britain.

0020-7683/87 $3.00+.00
Pergamon Journals Ltd.

DYNAMIC BUCKLING OF CYLINDRICAL SHELLS FROM OSCILLATING WAVES FOLLOWING AXIAL IMPACT

H. E. LINDBERG
APTEK, Inc., 4340 Stevens Creek Blvd., Suite 145, San Jose, CA 95129, U.S.A.

M. B. RUBIN
Israel Institute of Technology, Haifa, Israel

and

L. E. SCHWER
APTEK, Inc., 4340 Stevens Creek Blvd., Suite 145, San Jose, CA 95129, U.S.A.

(*Received* 30 *September* 1985)

Abstract—An experimental and theoretical investigation of dynamic buckling of thin cylindrical shells under oscillating stress waves following axial impact shows that hoop breathing response induced by the Poisson effect plays a strong role in initiating buckling, and that the stress oscillations allow buckling initially localized near the impacted end to propagate up the shell toward the free end. As a result of this energy spreading, the total compressive impulse of multipulse loading can be substantially larger than the critical impulse for a single pulse. The radial deformation of breathing provides a deterministic mechanism for initiation of symmetric buckling, which dominates early response for superclassical impact loads. For subclassical impact loads, the circumferential stress resultant from the Poisson effect excites hyperbolic growth of a large group of asymmetric modes; a continuous range of impact loads extending to values below the static classical buckling load therefore result in dynamic buckling within the scope of classical buckling theory with inertia terms added.

1. INTRODUCTION

The first extensive experiments on dynamic buckling of thin cylindrical shells under axial impact were performed by Coppa and Nash[1]. Most were performed by dropping weights onto rigidly supported test shells or by dropping shells, with masses attached at the upper end, into sand or water. In general, buckling occurred after several reverberations of axial stress waves up and down the shell, with the axial force increasing until buckling occurred. Axial force was recorded with back-to-back strain gages and buckle patterns were recorded by movies taken during selected experiments. However, the framing rate of the movies was too slow to record the onset of buckling, and in posttest photographs only the late-time plastic folding in longer wavelength modes was observable.

Almroth *et al.* [2] obtained excellent high-speed motion pictures of shells buckling dynamically following a small perturbation of a statically applied axial load. The photographs showed clearly that initial buckling was in a short wavelength pattern. After this pattern spread over the shell, a complex transition took place to a final static buckle pattern having wavelengths about twice those of the initial buckling.

Among the first analyses of dynamic buckling were those by Coppa and Nash[1] and also by Roth and Klosner[3]. The axial force was assumed to increase linearly with time (a reasonable idealization for multiple reverberations during impact at low velocity) and the shell was assumed to buckle into a few modes representative of the final static buckle pattern. The analyses were performed before the results in Ref. [2] were reported and no account was taken of any initial buckling into a shorter wavelength pattern. Hutchinson and Budiansky[4] proposed a method for relating the load reduction in dynamic buckling caused by shell imperfections to the reduction observed in static buckling of imperfect shells.

Dynamic buckling under higher velocity impact, such that the axial load increased abruptly to its maximum value immediately upon impact, was investigated by Lindberg and Herbert[5]. In these experiments, the shell was free at the end opposite the impact to eliminate any further increase in load from axial wave reverberations. As a result, very short wavelength buckles observed by ultra-high-speed movies were retained in the permanent buckle shape without obliteration by later quasi-static buckling and folding. Their analysis showed that buckling modes and critical load durations for this supercritical buckling can be predicted by classical shell buckling theory, and that the modes of buckling are random with statistics determined by the amplification of "white noise" imperfections.

Later, Schwieger and Spudia[6] performed experiments similar to those in Ref. [1]. Impact was by a spherical mass against an end plate attached to the shells. This ensured axial waves with a planar front perpendicular to the shell axis. Again, with the shell squeezed between a moving end mass and a fixed base, the load increased through a series of axial wave reverberations. They developed a lighting arrangement to obtain good resolution of developing buckle patterns in high-speed motion pictures.

Kornev and Solodovnikov[7] extended the theory in Ref. [5] to include the effect of finite velocity axial wave propagation. In essence, their approximate theory multiplied the buckle motion for infinite wave velocity, which is uniform along the shell length, by a decaying exponential function of position from the impacted end that accounts for the increased duration of buckle motion at points closer to the plane of impact. The exponent is the travelling wave counterpart to the exponential growth of buckles at any fixed position.

An analysis to account for axial load variation during buckling under reverberating axial stress waves was performed by Tamura and Babcock[8]. The analysis was analogous to that in Ref. [3] but with an added generalized coordinate in the fundamental axial vibration mode. Also, by analyzing buckling in a sequence of mode combinations, they showed a shift under dynamic loading to critical modes with wavelengths shorter than in static buckling, as well as demonstrating reductions in critical loads below those for static buckling. These were the experimental observations in Ref. [2].

The statistical approach in Ref. [5] was used by Maymon and Libai[9] to calculate the statistics of a stress quantity that they related to shell failure by dynamic buckling. Further experiments using an impact arrangement that gave a nearly square wave axial load similar to that in Ref. [5] were performed by Zimcik and Tennyson[10]. Their experimental results, along with theoretical calculations similar to those in Ref. [3], gave critical combinations of axial stress wave amplitude and duration to cause threshold buckling. This is similar to the result in Ref. [5] from dynamic analysis with classical shell theory, where the condition for threshold buckling was given as a critical value of dimensionless time, which in physical dimensions is proportional to the product of the magnitude and duration of the axial stress pulse.

In this paper, experimental and theoretical results are given for dynamic buckling of thin cylindrical shells under reverberating axial stress waves. The loading arrangement is as in Ref. [5], with the shells free at the end opposite the impact, but the shells are shorter so the reverberations result in several axial stress oscillations from compression to tension. With shorter shells and hence shorter compressive and tensile pulse durations, little buckling occurs during the initial compressive pulse at moderate stress levels. Also, the duration of hoop breathing oscillations, excited by the Poisson effect, is comparable to the axial pulse durations so circumferential as well as axial stress oscillations are important in the buckling response.

The investigation originated in the analysis of the more difficult but conceptually similar problem of impact of a thin, gently tapered conical shell. Similar phenomena are expected in the response of thin-walled tanks during earthquake loading. The modes of buckling are similar to those in Ref. [5] but the instrumentation and theoretical analysis are extended to study the nonlinear mutual interaction between buckle growth and axial stress wave propagation, including the reduction in resultant forces caused by buckle growth.

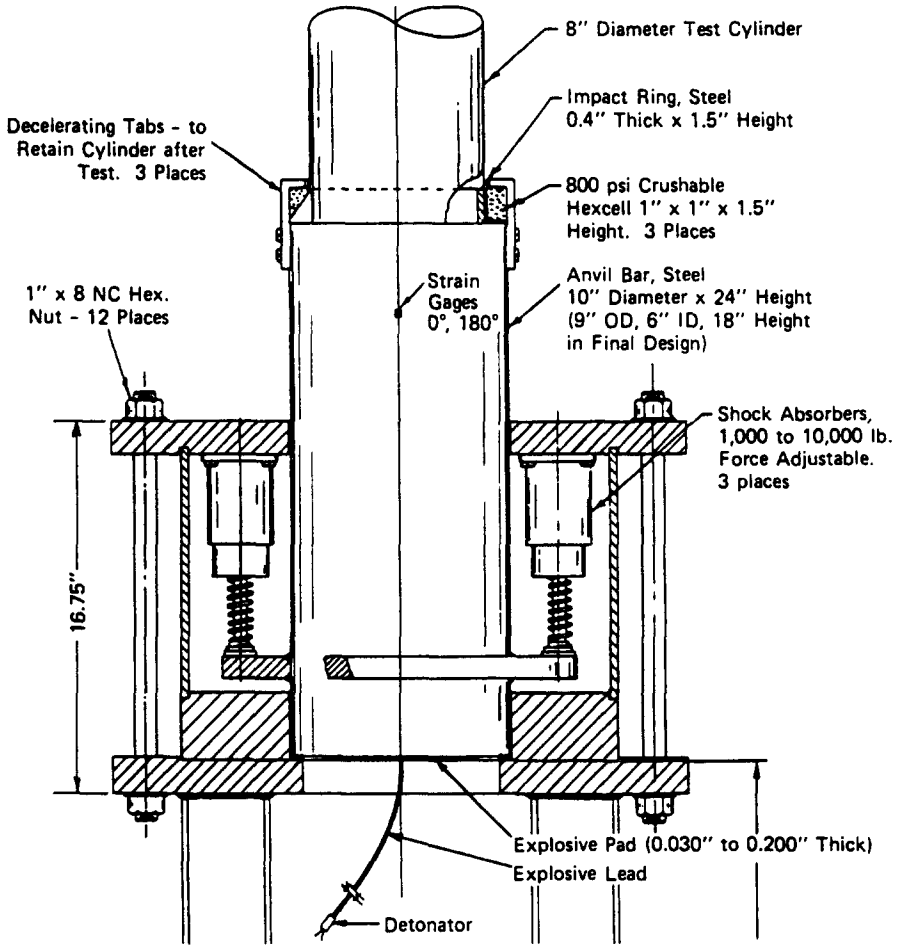

Fig. 1. Sketch of impact test apparatus.

2. EXPERIMENTAL ARRANGEMENT

The experimental arrangement is illustrated in Figs 1–4. Model shells were made of 8 mil thick (0.20 mm) sheets of titanium 6A1 4V alloy accurately cut to shape with an end mill, then rolled to an 8 in (203 mm) diameter and butt welded along the seam by a machine driven laser welder. Each shell was then attached to a massive internal end ring (called the impact ring in the figures) with epoxy and a band clamped around the outside of the shell. The other end of the shell was free. The unsupported length of the shells in the tests reported here was 13 in (330 mm).

The epoxy was applied by inverting the shell from the orientation shown in the figures, filling a conical paper trough around the massive ring with epoxy, and then, with the trough air-tight against the shell, pushing the ring slowly through the trough and into the shell. This procedure assured a bond with no voids to perturb a clamped boundary condition and was chosen over laser welding the shell to the ring to avoid deforming the shell through the inevitable tolerance gap between the shell and ring diameters.

The purpose of the apparatus shown in the figures is to impact the shell simultaneously around its circumference at an accurately known time. This was done by first placing the model shell and impact ring on top of a massive anvil bar, which had its upper surface accurately ground and lapped to mate with the impact ring, which was similarly ground and lapped. (To obtain higher impact velocities, the solid anvil bar indicated in Fig. 1 was replaced by an 18 in (0.47 m) long hollow shell about twice as thick as the impact rings.) Then a sheet of explosive was detonated at the base of the anvil bar, which drove a shock wave up the bar and into the impact ring. For an ideal step shock wave, the impact ring is accelerated to the particle velocity of the shock wave and is stress free as it imparts this

motion to the test shell. In practice, the ring had a small residual stress that resulted in a low amplitude, high frequency oscillation in the stress wave imparted to the shell, as seen in later figures.

The remainder of the apparatus was required to decelerate the anvil bar and deflect the blast wave from the explosive away from the test shell. Decelerating tabs with crushable Hexcell pads at three places around the impact ring were used to bring the test shell to rest without damage. Ring velocity was determined by using high-speed photography in a separate series of experiments with the ring free to fly away from the anvil bar. Ring velocity varied linearly with explosive thickness to velocities as high as 600 in s^{-1} (15.3 m s^{-1}) with the hollow, high-strength steel anvil bar.

High-speed photographs were taken with a Hycam motion picture camera operating with a quarter-frame optical head to obtain a framing rate of 40,000 frames per second. The lighting arrangement, adapted from Ref. [6] and illustrated in Figs 3 and 4, provided a series of vertical line images of the flash bulbs reflected from the shell surface. Line rather than point images were formed because of semi-diffuse reflection from the shiny but granular cylindrical surface. Because of the large lever distances from the camera objective lens to the shell and from the shell to the bulbs, the positions of the images were very sensitive to the slope of the shell at the location where the image is formed. Thus, very large magnification of shell bending motion was obtained. However, slope changes caused by symmetric buckles (axial bending) in the absence of asymmetric buckles (with circumferential bending) were difficult to observe because the displaced image simply rewrote on the line already illuminated by the line image.

Each shell was instrumented with 16 Micromeasurements Model EA-06-062AQ-350 [0.62 in (1.57 mm) gage length] strain gages. Back-to-back pairs, to measure both membrane and bending strain, were mounted on the outer and inner surfaces of the shell in the axial and circumferential directions at 0.60 in (15.2 mm) and at 6.5 in (165 mm) from the clamped boundary at the impact ring. These were supplemented by an array of four more outer surface axial gages surrounding the gages at 0.60 in, at close axial spacing (0.10 in = 2.5 mm) so that at least one gage was near a crest or trough of an axial buckle. Bending strain was deduced from these gages by knowing the membrane strain measured at the 0.60 in back-to-back pair and by a backup measurement of inside surface axial strain at 0.80 in. These gages were spread over a 20° arc of the shell and were connected to fine wires so as not to mass load the shell.

Axial gages were also located at $\pm 90°$ from the main array, to verify the uniformity of impact, and on the impact ring to further monitor the high frequency stress perturbations from the non-ideal explosive shock wave. The strain records were synchronized with the motion pictures to within a few microseconds by recording an optical marker of the explosive detonation on the film and a corresponding electrical pulse on the strain records.

3. THEORY OF INITIAL PULSE BUCKLING

Most of the detailed comparisons between theory and experiment given in the next section are made with the finite element code WHAMS[11], to allow inclusion of the mutual interaction between buckle growth and axial wave propagation. However, this analysis is limited to symmetric buckling, to avoid the currently prohibitive number of elements required to resolve buckle patterns with circumferential as well as axial waves. In the present section we summarize a closed form analysis for buckling under constant membrane forces, without reduction caused by buckling, which is similar to the analysis in Ref. [5]. This is done to show the nature of complete symmetric and asymmetric buckling and to demonstrate why the finite element analysis of only symmetric motion captures the most significant aspects of buckling in the present problem. We analyze motion only during the first compressive pulse, which has a duration equal to the transit

Fig. 2. Overview of test apparatus.

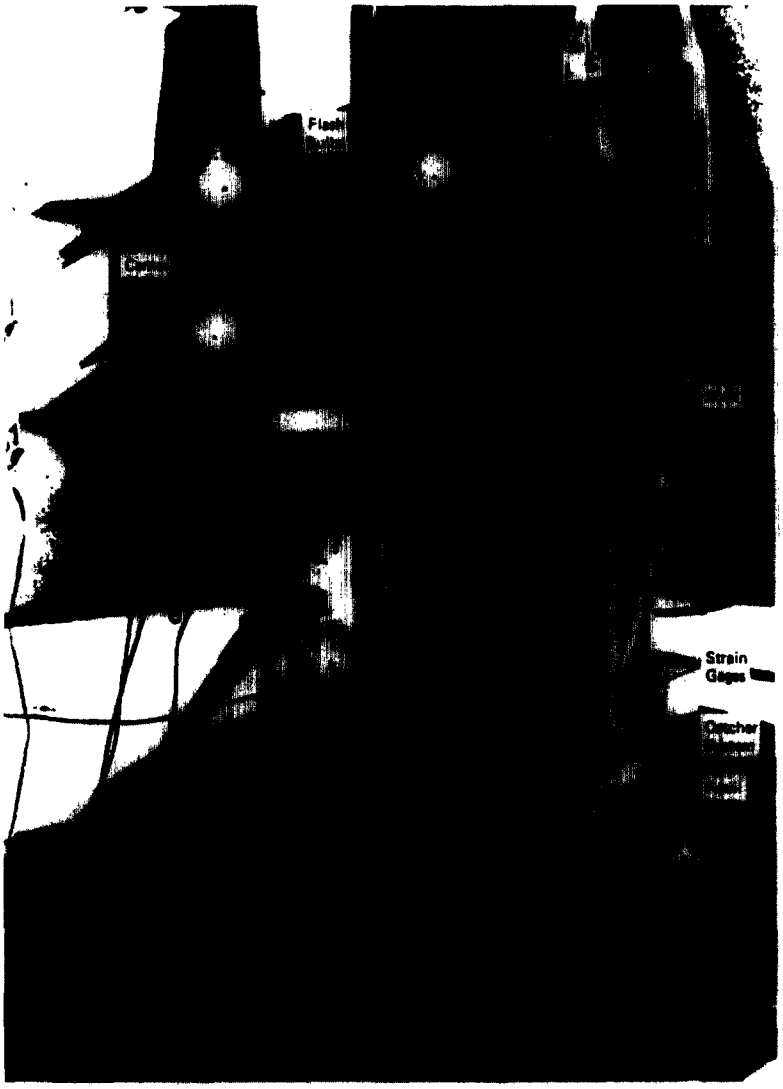

Fig. 3. Close-up of test model and photographic arrangement.

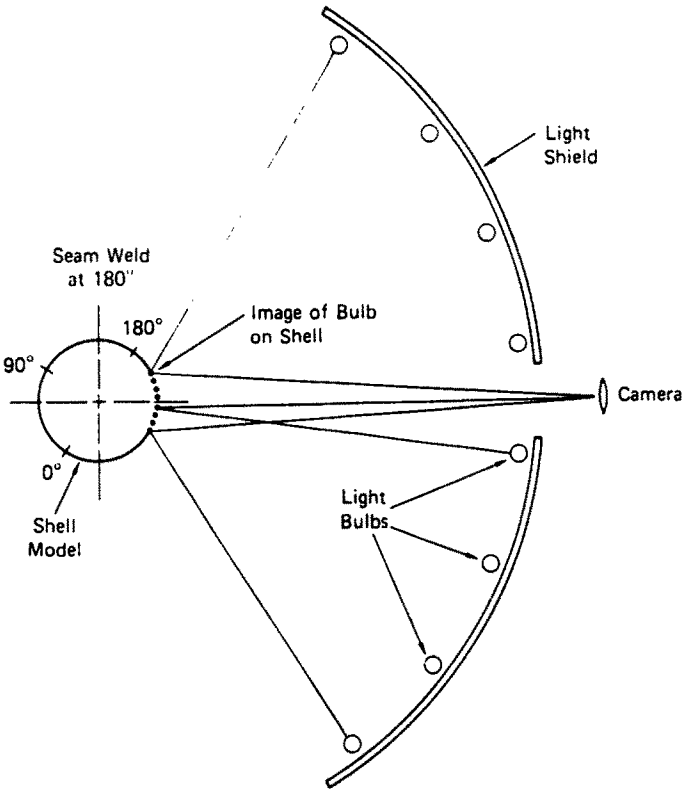

Fig. 4. Lighting arrangement.

time of the compressive impact force up the shell to the free end, plus the transit time of a relief wave from the free end back down to the impact ring.

For this purpose, we use the Donnell shell equations

$$D\nabla^4 w + \left[\bar{N}_x \frac{\partial^2}{\partial x^2} + \bar{N}_\theta \frac{\partial^2}{a^2 \partial \theta^2}\right](w + w_i) + \frac{\bar{N}_\theta}{a} - \frac{1}{a}\frac{\partial^2 F}{\partial x^2} + \rho h \frac{\partial^2 w}{\partial t^2} = 0 \tag{1}$$

$$\nabla^4 F = -\frac{Eh}{a}\frac{\partial^2 w}{\partial x^2} \tag{2}$$

$$\nabla^4( ) = \left(\frac{\partial^2}{\partial x^2} + \frac{1}{a^2}\frac{\partial^2}{\partial \theta^2}\right)^2( ) \tag{3}$$

where $w(x, \theta, t)$ is radial displacement, positive inward from an initial imperfection shape $w_1(x, \theta)$, x and θ are axial and circumferential coordinates, t is time, a, h and ρ are shell radius, thickness, and density, respectively, $D = Eh^3/12(1 - \nu^2)$ is the shell stiffness, E is Young's modulus, ν is Poisson's ratio, $\bar{N}_x$ and $\bar{N}_\theta$ are axial and circumferential stress resultants, positive in compression, and F is a stress function for stress resultants caused by stretching during deformation w. The bars over $\bar{N}_x$ and $\bar{N}_\theta$ denote that these are from applied loads, which are assumed to be known; the stretching components are omitted from these coefficients because they are linear in small deformation w and result in higher order terms. These equations can be found in many texts; a complete derivation is given in Ref. [12].

For simplicity, we assume simply supported end conditions

$$w = 0, \qquad \frac{\partial^2 w}{\partial x^2} = 0 \qquad \text{at } x = 0, L. \tag{4}$$

This is a reasonable simplification because the wavelengths of buckling are very short compared with the shell length and the boundary effect is local. In the finite element analysis discussed in the next section, a clamped boundary condition is used, which better approximates the clamping arrangement of the impact ring to the shell. Further, the shell is initially at rest, so

$$w = 0, \qquad \frac{\partial w}{\partial t} = 0 \qquad \text{at } t = 0. \tag{5}$$

Boundary conditions (4) are satisfied by the Fourier series

$$w_i(x, \theta) = \sum_{m=1}^{\infty} \sum_{n=0}^{\infty} a_{mn} \sin \frac{m\pi x}{L} \cos n\theta \tag{6}$$

$$w(x, \theta, t) = \sum_{m=1}^{\infty} \sum_{n=0}^{\infty} w_{mn}(t) \sin \frac{m\pi x}{L} \cos n\theta \tag{7}$$

$$F(x, \theta, t) = \sum_{m=1}^{\infty} \sum_{n=0}^{\infty} F_{mn}(t) \sin \frac{m\pi x}{L} \cos n\theta \tag{8}$$

where w_{mn} and F_{mn} are functions of time to be determined and a_{mn} are the Fourier coefficients of the initial imperfections. To also represent the term $\bar{N}_\theta/\rho ha$ in the Fourier series, we introduce b_{mn} as the expansion of unity

$$1 = \sum_{m=1}^{\infty} \sum_{n=0}^{\infty} b_{mn} \sin \frac{m\pi x}{L} \cos n\theta \tag{9}$$

from which

$$b_{mn} = \begin{cases} \dfrac{2}{m\pi}[1 - (-1)^m], & \text{for } n = 0 \\ 0, & \text{for } n \neq 0. \end{cases} \tag{10}$$

Substitution of eqns (6)–(9) into eqns (1) and (2) and use of the orthogonality properties of the functions $\sin m\pi x/L$ and $\cos n\theta$ gives the following equations of motion:

$$\frac{d^2 w_{mn}}{dt^2} + k_{mn} w_{mn} = \left[\frac{\bar{N}_x \mu^2}{\rho h} + \frac{\bar{N}_\theta \eta^2}{\rho h}\right] a_{mn} - \frac{\bar{N}_\theta}{\rho ha} b_{mn} \tag{11}$$

where

$$k_{mn} = \frac{D}{\rho h}(\mu^2 + \eta^2)^2 - \frac{\bar{N}_x \mu^2}{\rho h} - \frac{\bar{N}_\theta \eta^2}{\rho h} + \frac{E\mu^4}{\rho a^2}(\mu^2 + \eta^2)^{-2} \tag{12}$$

and

$$\mu = \frac{m\pi}{L}, \qquad \eta = \frac{n}{a}. \tag{13}$$

From eqn (11) we realize that the solution for w_{mn} separates into two parts: one part, w'_{mn}, satisfies the equation

$$\frac{d^2 w'_{mn}}{dt^2} + k_{mn} w'_{mn} = \left[\frac{\bar{N}_x \mu^2}{\rho h} + \frac{\bar{N}_\theta \eta^2}{\rho h}\right] a_{mn} \tag{14}$$

and is associated with the random imperfections in the shell. In eqn (14), there is no sum implied by the repeated indices. The other part, w^d_{mn}, satisfies the equations

$$\frac{d^2 w^d_{m0}}{dt^2} + k_{m0} w^d_{m0} = -\frac{\bar{N}_\theta}{\rho h a} b_{m0}$$

$$w^d_{mn} = 0, \qquad \text{for } n \neq 0 \tag{15}$$

and is an axisymmetric solution that is deterministic. The complete solution is given by

$$w_{mn} = w^r_{mn} + w^d_{mn} \tag{16}$$

where each part satisfies initial conditions (5). The part w^d_{mn} is deterministic because it results directly from response of the shell and occurs even in the absence of imperfections. This buckling is initiated by bending that occurs near the supported end of the shell as it expands in response to the circumferential resultant force N_θ. Because the applied loads are assumed to be spatially uniform, the deterministic solution is in axisymmetric modes only ($n = 0$).

We assume for simplicity in the present analysis that the impact load is instantly uniform throughout the length of the shell. This is a useful assumption if we focus our attention on a few buckle waves near the impacted end of the shell, where the load is indeed nearly instantaneously applied and then constant for the total duration of the compression pulse. Then the loading quantities are given by

$$\bar{N}_x = \bar{N}, \qquad \bar{N}_\theta = \gamma \bar{N} \tag{17}$$

where $\bar{N}$ is a constant defining the magnitude of the load and γ is a constant defining the relative magnitudes of $\bar{N}_x$ and $\bar{N}_\theta$. For a relatively short shell, as in the experiments here, we specify $\gamma = \nu$, because $\bar{N}_\theta$ has a duration comparable to the duration of $\bar{N}_x$. This occurs because $\bar{N}_\theta$ results from the Poisson effect and has a duration, as the shell expands radially to relieve the hoop force, proportional to the shell diameter. For a relatively long shell, as in Ref. [5], we specify $\gamma = 0$, because the circumferential resultant is relieved in a short time compared with the duration of the axial force resultant.

The solutions for w^r_{mn} and w^d_{mn} are then given by

$$w^r_{mn} = g_{mn} a_{mn} \tag{18}$$

where g_{mn} is an amplification function given by

$$g_{mn} = \frac{\bar{N}(\mu^2 + \gamma\eta^2)}{\rho h}\left[-\frac{1}{k_{mn}}\begin{pmatrix}\cosh\\ \cos\end{pmatrix}|k_{mn}|^{1/2} t - 1\right)\right] \tag{19}$$

and the deterministic solution is

$$w^d_{m0} = \frac{\gamma \bar{N} b_{m0}}{\rho h a}\left[\frac{1}{k_{m0}}\begin{pmatrix}\cosh\\ \cos\end{pmatrix}|k_{m0}|^{1/2} t - 1\right)\right]. \tag{20}$$

The hyperbolic functions are used for $k_{mn} < 0$ and the trigonometric functions are used for $k_{mn} > 0$. The total functions in the square brackets are replaced by $t^2/2$ for $k_{mn} = 0$.

The load $\bar{N}_{tr}$ associated with the transition from trigonometric behavior to exponential growth in eqns (19) and (20) is determined by setting $k_{mn} = 0$. It then follows from eqn (12) that

$$\bar{N}_{tr} = \frac{(EhD)^{1/2}}{a}\left(\frac{1}{1+\gamma\beta^2}\right)\left(Q + \frac{1}{Q}\right) \tag{21}$$

where

$$Q = \left(\frac{Da^2}{Eh}\right)^{1/2}\mu^2(1+\beta^2)^2, \qquad \beta = \frac{\eta}{\mu}. \tag{22}$$

If L and a are large enough, then μ and η can be approximated by continuous variables and expression (21) can be minimized with respect to the variables Q and β^2. With attention confined to only the axial loading component ($\gamma = 0$), eqn (21) reduces to the expression for the classical static axial buckling load $\bar{N}_{cl}$

$$\bar{N}_{cl} = \frac{2(EhD)^{1/2}}{a} = \frac{Eh^2}{a}\frac{1}{\sqrt{(3(1-\nu^2))}} \tag{23}$$

in which eqn (21) is minimized by $Q = 1$ for $\gamma = 0$.

With both circumferential and axial compressive loads present, as in the impact problem here, $\gamma > 0$ and $\bar{N}_{tr}$ can be substantially less than the classical buckling load $\bar{N}_{cl}$ for a range of axial and circumferential mode numbers. To see this, we note that for continuous values of Q and β^2 eqn (21) can be minimized with respect to Q to obtain the same result $Q = 1$. For this value of Q the minimum value of $\bar{N}_{tr}$ approaches zero as β approaches infinity and μ approaches zero. However, since m is a positive integer, the minimum value of μ is π/L (for $m = 1$) and an estimate of the critical buckling load N_{cr} associated with the minimum value of $\bar{N}_{tr}$ becomes

$$\frac{\bar{N}_{tr}}{\bar{N}_{cl}} = \frac{1}{1+\gamma\beta^2_{max}} \tag{24}$$

where $\bar{N}_{cl}$ is given by eqn (23) and β^2_{max} is determined by setting $Q = 1$ in eqn (22) and taking the minimum value of μ to obtain

$$\beta^2_{max} = \left(\frac{Eh}{Da^2}\right)^{1/4}\left(\frac{L}{\pi}\right) - 1. \tag{25}$$

If the right-hand side of eqn (25) is negative, then the critical buckling load is estimated by

$$\frac{\bar{N}_{cr}}{\bar{N}_{cl}} = \frac{1}{2}\left(Q + \frac{1}{Q}\right), \qquad Q = \left(\frac{Da^2}{Eh}\right)\left(\frac{\pi}{L}\right)^2 \tag{26}$$

which is associated with a symmetric mode ($\beta = 0$, $\eta = 0$).

Actually, since n is an integer, the exact critical value $\bar{N}_{cr}$ is determined by evaluating eqn (21) with $m = 1$ and n equal to an integer value near the value obtained with eqns (13), (22) and (25) when eqn (25) is applicable, or n near zero when eqn (26) is applicable. (Only values of n equal to about 4 or larger are appropriate with these Donnell-type equations, in order that the shallow-shell approximation is reasonably accurate.) For the shell discussed in Section 4 with $\gamma = 0.3$, one finds that the exact critical value is $\bar{N}_{cr}/\bar{N}_{cl} = 0.204$ for $m = 1$, $n = 4$. In the experiments discussed in Section 4, the impact load is higher than this critical load and a wide range of modes grow exponentially even for the experiment in which the load is less than the classical buckling load $\bar{N}_{cl}$.

The features of the amplification function (19) for random imperfections are illustrated in Fig. 5 for a shell similar to those in the experiments. The axial impact load in all the

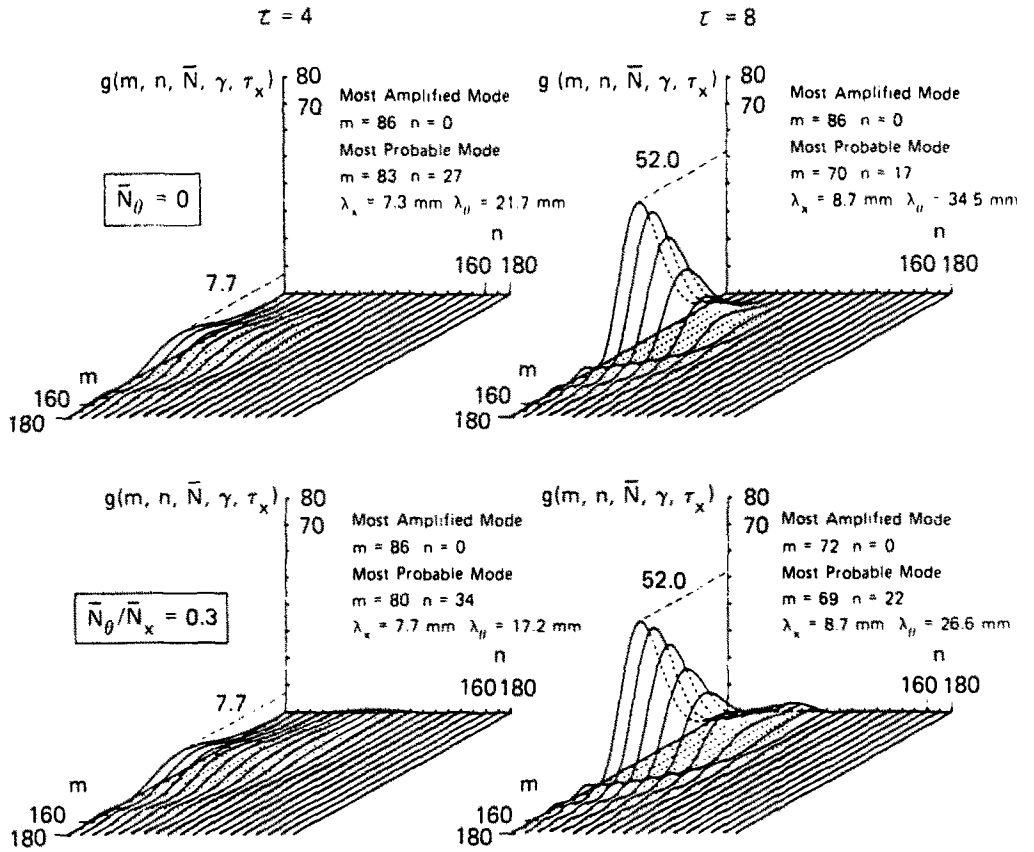

Fig. 5. Amplification functions for long shell ($\gamma = 0$) and short shell ($\gamma = 0.3$) single-pulse limits [$L = 305$ mm, $2a = 187$ mm, $h = 0.20$ mm, $\bar{N}(1 - \nu^2)/Eh = 0.0033$].

examples is $\bar{N}(1 - \nu^2)/Eh = 0.0033$, which for the example shell gives $\bar{N}/\bar{N}_{cl} = 2.6$. In each graph, continuous curves of g_{mn} are plotted against m at a sequence of values of n, which shows the humped nature of the surface representing g_{mn}.

The upper two graphs are for $\gamma = 0$ at dimensionless times of $\tau = 4$ and 8, where $\tau = \bar{N}t/(\rho h D)^{1/2}$ as defined in Ref. [5]. As in the examples in Ref. [5], for this case a large number of modes are amplified with mode numbers extending over a substantial range of both m and n. The most amplified mode is a symmetric mode ($n = 0$) and has an amplification of 52 at $\tau = 8$. However, the most probable modes have $m = 83$ and $n = 27$ at $\tau = 4$ and $m = 70$ and $n = 17$ at $\tau = 8$. These are the wave numbers corresponding to the most probable wavelengths that would be observed for white noise initial imperfections (see Ref. [5]). The corresponding wavelengths, given in the figure, are quite short compared with the size of the shell.

The lower two graphs are for $\gamma = 0.3$ and assume that no relief of $\bar{N}_\theta$ takes place during the axial pulse duration. The actual motion is between these extremes in γ. However, even with this upper limit of γ for axial impact, the basic nature of the amplification function is similar to that in the upper two graphs for $\gamma = 0$. A "hump" of modes are amplified and the maximum amplification is in a symmetric mode and has the same values as for $\gamma = 0$. The main difference is that the range of amplified modes extends to somewhat larger values of n (shorter circumferential buckle wavelengths). This is particularly noticeable for the fundamental axial mode number $m = 1$. As a result, the most probable modes are shifted to shorter circumferential wavelengths, with $m = 80$ and $n = 34$ at $\tau = 4$ and $m = 69$ and $n = 22$ at $\tau = 8$. This shift is quite small.

For this case, in which $\bar{N}$ is greater than $\bar{N}_{cl}$, the predominant effect of $\bar{N}_\theta$ is that it introduces a deterministic, symmetric component of buckling as given by eqn (20), so that buckling occurs even in the absence of imperfections. Thus, for accurately made shells

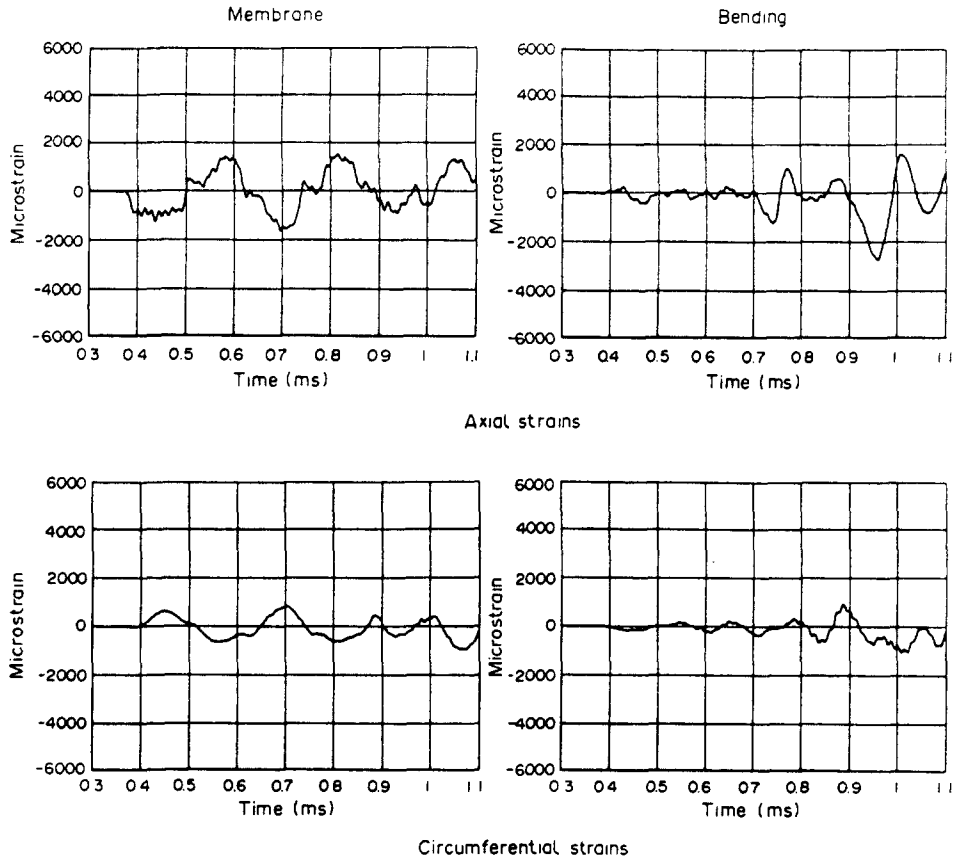

Fig. 6. Experimental strains at $x = 15.2$ mm for axial impact at 4.93 m s^{-1} [$\bar{N}(1 - \nu^2)/Eh = 0.0010$, $\bar{N}/\bar{N}_{cl} = 0.87$].

under high stress, short duration loading, buckling in symmetric modes is expected to play a significant role. We will see in the next section that an analysis that includes only symmetric modes correlates well with experimental results. For lower velocity impact, such that $\bar{N} < N_{cl}$, the predominant effect of $\bar{N}_\theta$ is to induce hyperbolic growth of asymmetric buckle modes as discussed above, so dynamic buckling occurs even for subclassical impact loads.

4. COMPARISON OF EXPERIMENTAL AND THEORETICAL RESULTS

4.1. *Subclassical impact load*

Figure 6 gives experimental membrane and bending strain records at a location 0.60 in (15.2 mm) above the clamped boundary at the impact ring for an impact velocity of 4.93 m s^{-1}. The corresponding impact strain, as recorded by the gages, is $\bar{N}(1 - \nu^2)/Eh = 0.0010$. The force resultant is $\bar{N}/\bar{N}_{cl} = 0.87$.

Since the applied force resultant is below $\bar{N}_{cl}$, little buckling occurs during the first cycle of axial compression and tension and the nature of the applied loading is clear. The axial membrane strain increases abruptly in compression at the time of initial "impact" by the impact ring. Time in the figure (and in all the experimental and theoretical strain and photographic records in subsequent figures) is measured from the instant the detonator was fired to initiate the explosive pad. The time from this instant until the stress wave arrives at the base of the shell is 0.328 ms.

The rectangular wave feature of the first compression pulse is clearly evident. Its duration is 0.12 ms, the time for a compressive wave to propagate up the shell from the strain gage location to the free end, and a returning tensile relief wave to propagate back

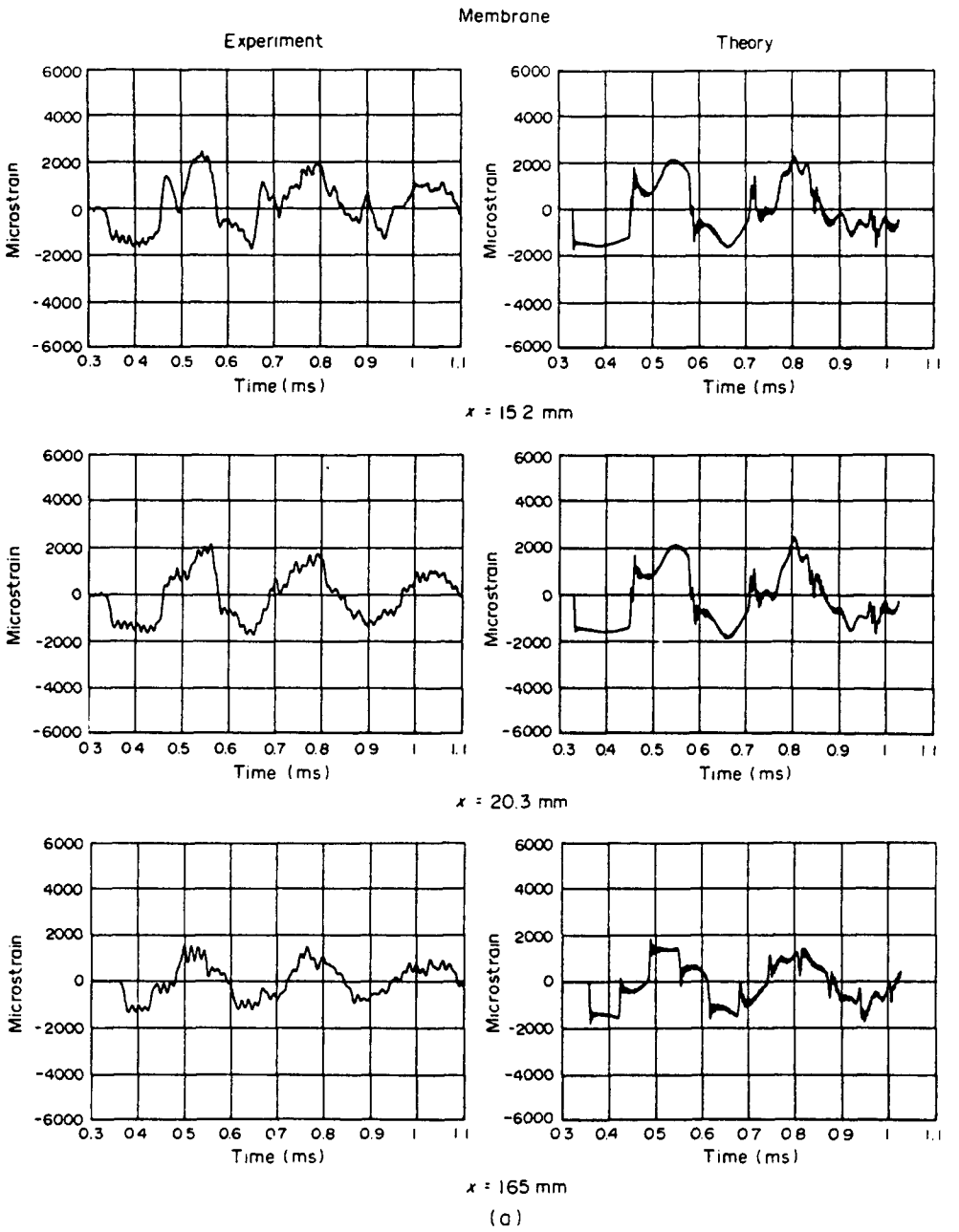

Fig. 7. Comparison of experimental and theoretical axial strains for axial impact at 7.42 m s^{-1} [$\bar{N}(1-\nu^2)/Eh = 0.0015$, $\bar{N}/\bar{N}_{cl} = 1.31$].

down to the strain gage. When the tensile wave reflects from the massive impact ring as an upward propagating tensile wave, it suddenly changes the strain at the gage location to tension.

In a simple bar, the tensile pulse would be a rectangular pulse just opposite in sign from the compression pulse. For the shell, the tensile pulse has a sine wave superimposed on this rectangular pulse so that at first it is smaller than the compressive pulse and then it is larger. This is the Poisson effect of symmetric breathing expansion and contraction of the shell. This is more clearly evident in the theoretical membrane strain for another example in Fig. 7. It so happens that, in these shells, the period of this breathing is very nearly equal to the axial pulse duration because the circumference of the shell is nearly equal to twice its length.

Superimposed on the strain record is a high frequency wiggle. This is the result of the finite rise time of the stress wave driven into the impact ring by the explosively loaded

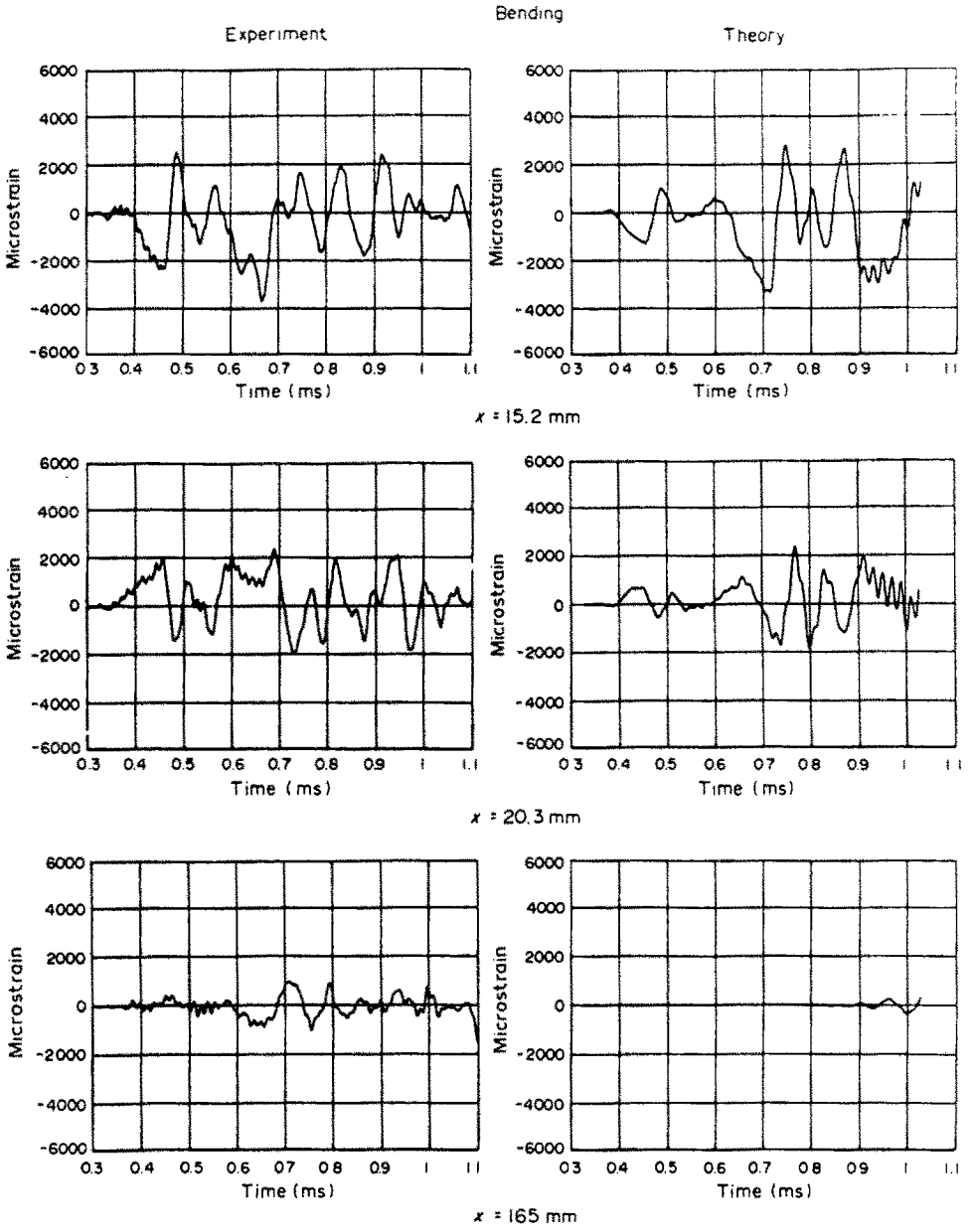

Fig. 7(b).

anvil bar, as discussed previously. In the theoretical calculations, to compare with each experiment, the initial velocity of the shell toward a rigid mass was taken such that the impact strain was the measured axial membrane strain through the average peaks of this ripple.

The remainder of the axial membrane strain record in Fig. 6 clearly shows a succession of three oscillations from compression to tension. The axial bending strain record shows that little bending occurs during the first compression, but then a pulse of bending occurs during the second compression and this bending is further amplified during the third compression. This extraction of bending energy is reflected by a decrease in the membrane strain from the second compression to the third.

The circumferential membrane strain in Fig. 6 clearly shows the hoop breathing oscillation of the shell. The circumferential bending strain has features similar to those of the axial bending strain but with smaller amplitudes.

The axial and circumferential bending is attributed to dynamic buckling in asymmetric modes. This occurs because, while the axial force resultant is below the classical static

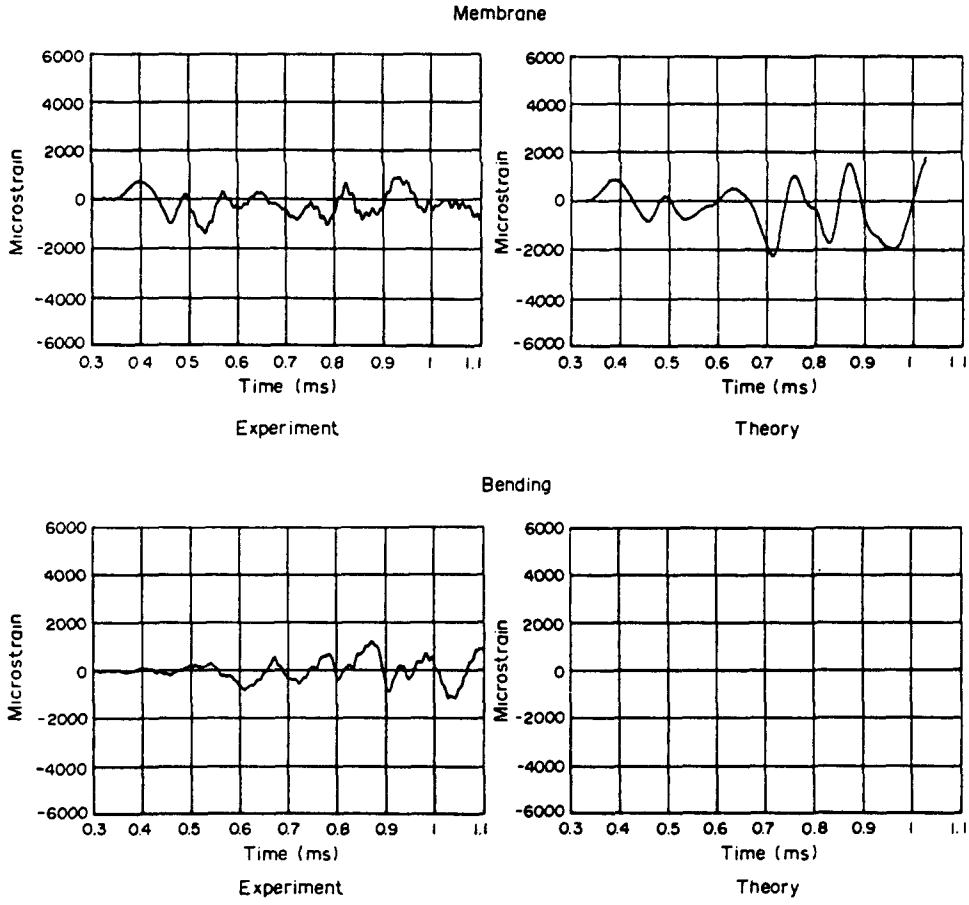

Fig. 8. Comparison of experimental and theoretical circumferential strains at $x = 15.2$ mm for axial impact at 7.42 m s^{-1} ($\bar{N}/\bar{N}_{cl} = 1.31$).

buckling value, the circumferential force resultant induced by the Poisson effect results in a dynamic load combination that is supercritical for a large group of asymmetric modes [see discussion of eqn (21)].

With this subclassical impact load, calculation of an amplification function similar to that given in Fig. 5 shows a group of modes with amplitudes growing rapidly with time. While the wavelengths of these modes are longer than in Fig. 5, they are nevertheless short compared with those for static buckling and are shorter in the axial direction than in the circumferential direction because $\bar{N}_x$ is substantially larger than $\bar{N}_\theta$. Shorter wavelengths in the axial direction are reflected by the axial bending strain in Fig. 6 being larger than the circumferential bending strain.

To obtain good theoretical predictions of buckling for this subclassical load, it would be necessary to model the asymmetric modes initiated by shell imperfections. This is because these asymmetric modes become more significant, relative to the deterministic symmetric modes, for subclassical loads than for superclassical loads. Since the number of finite elements necessary to predict short-wavelength asymmetric buckles is prohibitive at present, no theoretical predictions are presented for this experiment.

4.2. *Superclassical impact load*

Figures 7 and 8 give a more complete set of strain records for a higher impact velocity such that $\bar{N}/\bar{N}_{cl} = 1.31$. With this superclassical loading, symmetric modes of buckling are highly unstable as discussed in Section 3. With radial expansion of the shell away from the clamped boundary as a deterministic mechanism for initiating symmetric buckling, symmetric modes are expected to dominate response. These can be modeled at the high

axial spatial resolution required for the very short wavelengths of dynamic buckling with a single row of closely-spaced finite ring elements.

Response was calculated with the finite element code WHAMS, which was developed at the University of Illinois at Chicago Circle for transient analysis of two-dimensional structures. A key feature of the code is that the governing equations are formulated with rigidly convected element coordinates to treat large displacements with small strains. These introduce the geometric nonlinearities needed to analyze dynamic buckling. Material properties used in the calculations for the titanium alloy are $\rho = 4.52\,\mathrm{Mg\,m^{-3}}$, $E = 110\,\mathrm{GPa}$, and $\gamma = 0.3$.

The first group of plots in Fig. 7 compare experimental and theoretical results for axial membrane strain. The second group compare axial bending strains. Each comparison is made at axial gage locations of 15.2, 20.3, and 165 mm from the impact ring support. The value of τ at the end of the first axial compression pulse is 20, but it is clear from the bending strain histories that substantial buckling takes place by about half this value, consistent with the conservative estimate in Ref. [5] that observable buckling takes place by about $\tau = 7$ for a single pulse.

During the second compressive pulse, buckling from the first pulse is further amplified such that much of the membrane strain energy of wave propagation has been converted to bending. Beyond this time both bending and membrane response are simply oscillatory. All of these features of wave propagation, buckling, and oscillations are quite well reproduced by the theoretical results.

The gages at the two locations close to the impacted end of the shell both show an identical sequence of events, but the initial bending at the 15.2 mm gage pair is in compression while the initial bending at the 20.3 mm gage pair is in tension. Records from the complete set of five closely-spaced gages demonstrated that the gages discussed here were located close to a crest and trough of a buckle wave. Buckle wavelength deduced from these records and from the motion pictures was about 15 mm.

Records from the gage pair at 165 mm, half way up the shell, show the more complex compressive strain history at this location and also that the bending amplitude is much reduced. This is because the buckling takes place mainly near the impacted end of the shell, where the compressive pulses occur first and are longest, and extracts energy from the membrane wave propagation. The theoretical results show essentially no buckling at the midheight of the shell. However, later in time, the bending initiated by the buckling near the impacted end propagates up the shell as bending waves. The time window in the figure is too short to show this bending.

The circumferential membrane strain, in Fig. 8, has many of the features of the membrane strain in Fig. 6 for the lower loading amplitude. The circumferential bending strain is substantially lower than the axial bending strain, as observed at the lower loading, demonstrating that the buckle axial wavelengths are shorter than the circumferential wavelengths. In this case, the circumferential bending is nearly zero during the first compressive axial pulse, confirming that symmetric buckling dominates early response.

Figure 9 gives the high-speed motion pictures from this experiment. The camera view shows only a little less than half the projected width of the shell (a 54° arc about the centerline of the shell). Also, in the cropped prints in the figure, only half the 330 mm height of the shell is seen. The indications of compression and tension given in Fig. 9 are based on the time spans of compressive and tensile axial strains at $x = 0.60$ taken from Fig. 7.

The appearance of buckles with increasing time is apparent. Closer examination shows that buckling during the first compression pulse is dominated by symmetric buckles, because the buckles are barely detectable even though from Fig. 7 we know that the strains are just as large as in the second and third compression, during which the photographs show wildly dancing reflected image lines. The latter feature of the photographs is caused by the very large amplification of circumferential slope changes as recorded by the image line positions. Similar axial slope changes go undetected in the absence of circumferential bending (i.e. during symmetric buckling) as discussed in Section 2. The wild wiggles in the

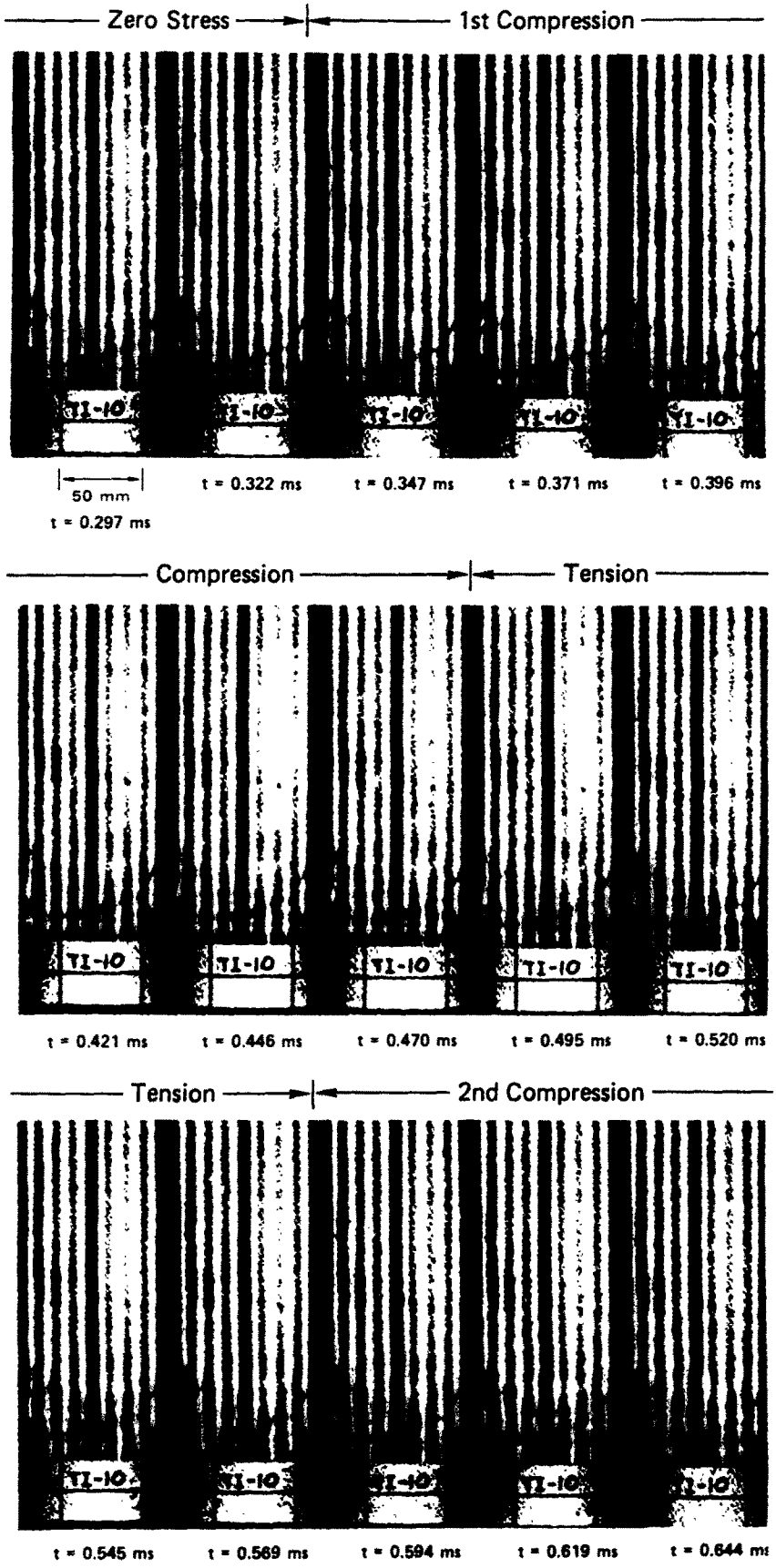

Fig. 9. High-speed motion pictures of cylindrical shell buckling under reverberating axial impact stress waves (same experiment and time base as in Figs 7 and 8).

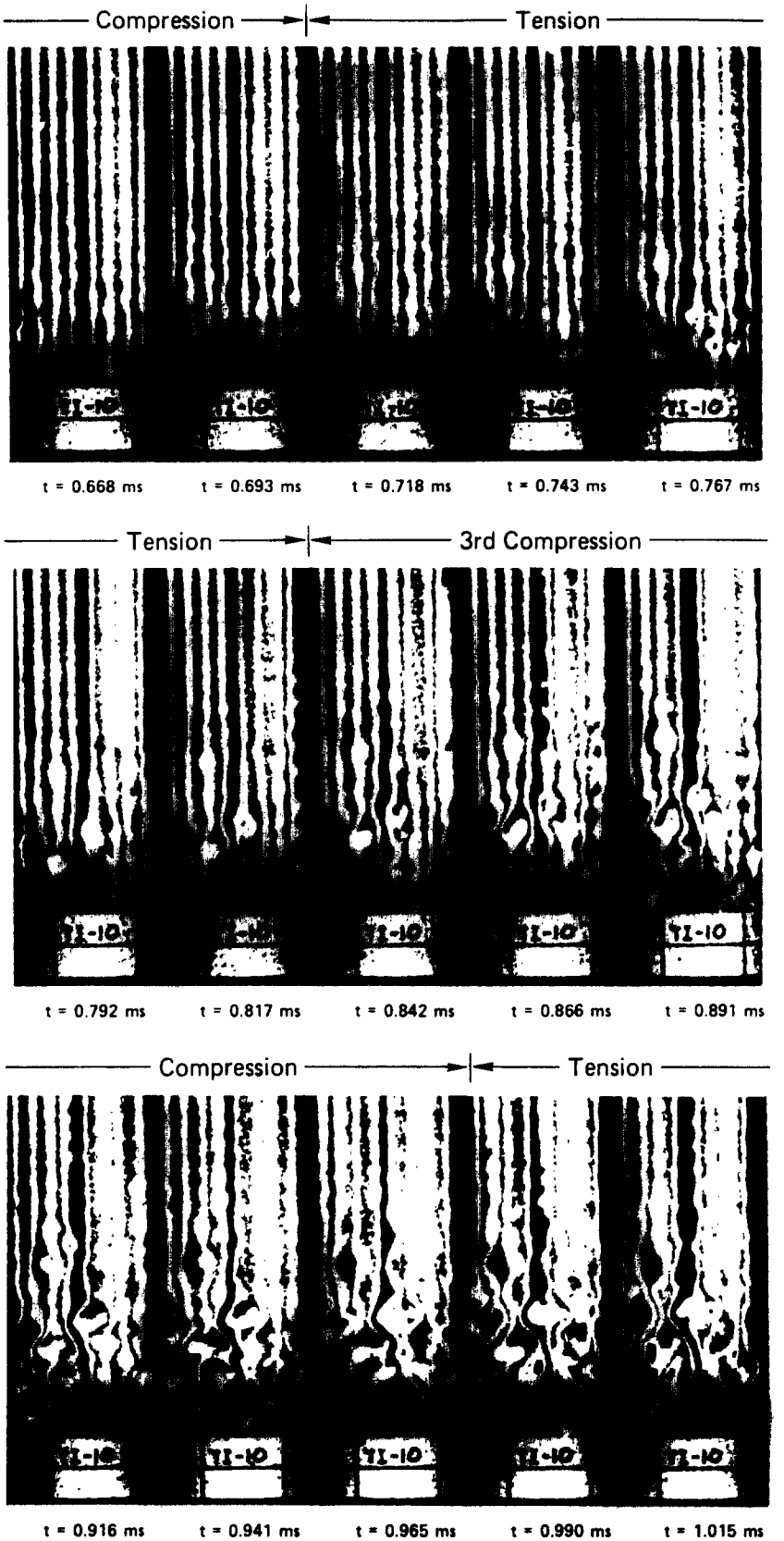

Fig. 9. Continued.

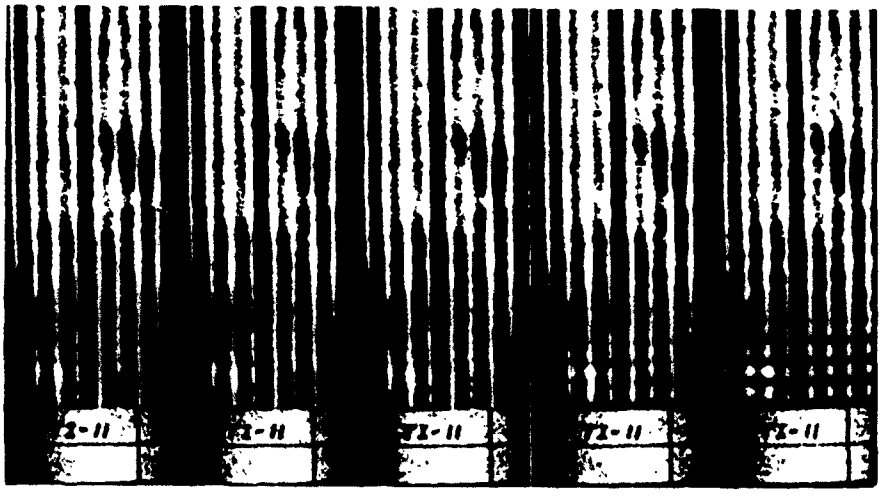

Fig. 11. Motion pictures of cylindrical shell buckling under axial impact at 12.4 m s^{-1} [$\bar{N}(1-\nu^2)/Eh = 0.0025$, $\bar{N}/\bar{N}_{cl} = 2.19$].

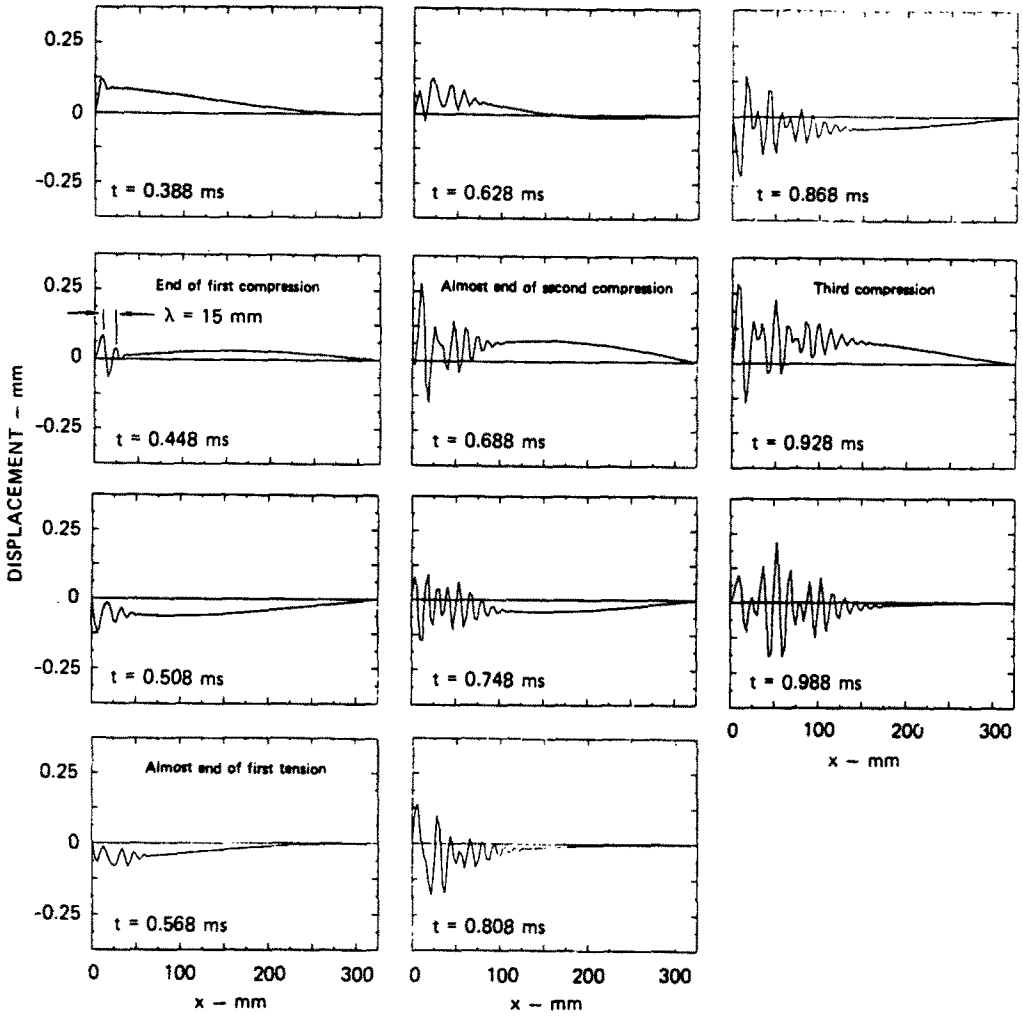

Fig. 10. Calculated radial displacement (positive outward) for axial impact at 7.42 m s^{-1} (times are shifted to correspond with experimental results in Figs 7–9).

reflected line images correspond to only modest buckle amplitudes; the shell returned to its original shape after the test so all of the buckling was elastic.

Another feature of multipulse buckling that can be seen upon closer inspection is that the buckles grow during the first and second axial compressive pulses and propagate up the shell as bending waves during the intervening axial tensile pulses. This is because the motion changes from hyperbolic to trigonometric (from growth with fixed wave positions to oscillations with bending wave propagation) as the sign of k_{mn} changes in the equations of motion.

This feature of the motion is even more apparent in the calculated buckle shapes in Fig. 10, which are from the same calculations made for the strains in Figs 7 and 8. All of the features of buckle growth and bending wave propagation up the shell are vividly apparent. The buckling is closely contained near the impacted end of the shell during the first compression and has a wavelength of 15 mm, in agreement with measurements from the strain records and photographs. Near the end of the first tension, waves have propagated about a quarter the way up the shell. These grow during the second compression and then propagate to about half way up the shell by the third compression. Thus, as observed from the strain records, little bending strain occurs at the center of the shell until later in time. Note also that the displacements are quite small, with a maximum value about equal to the wall thickness (1/500th of the shell radius).

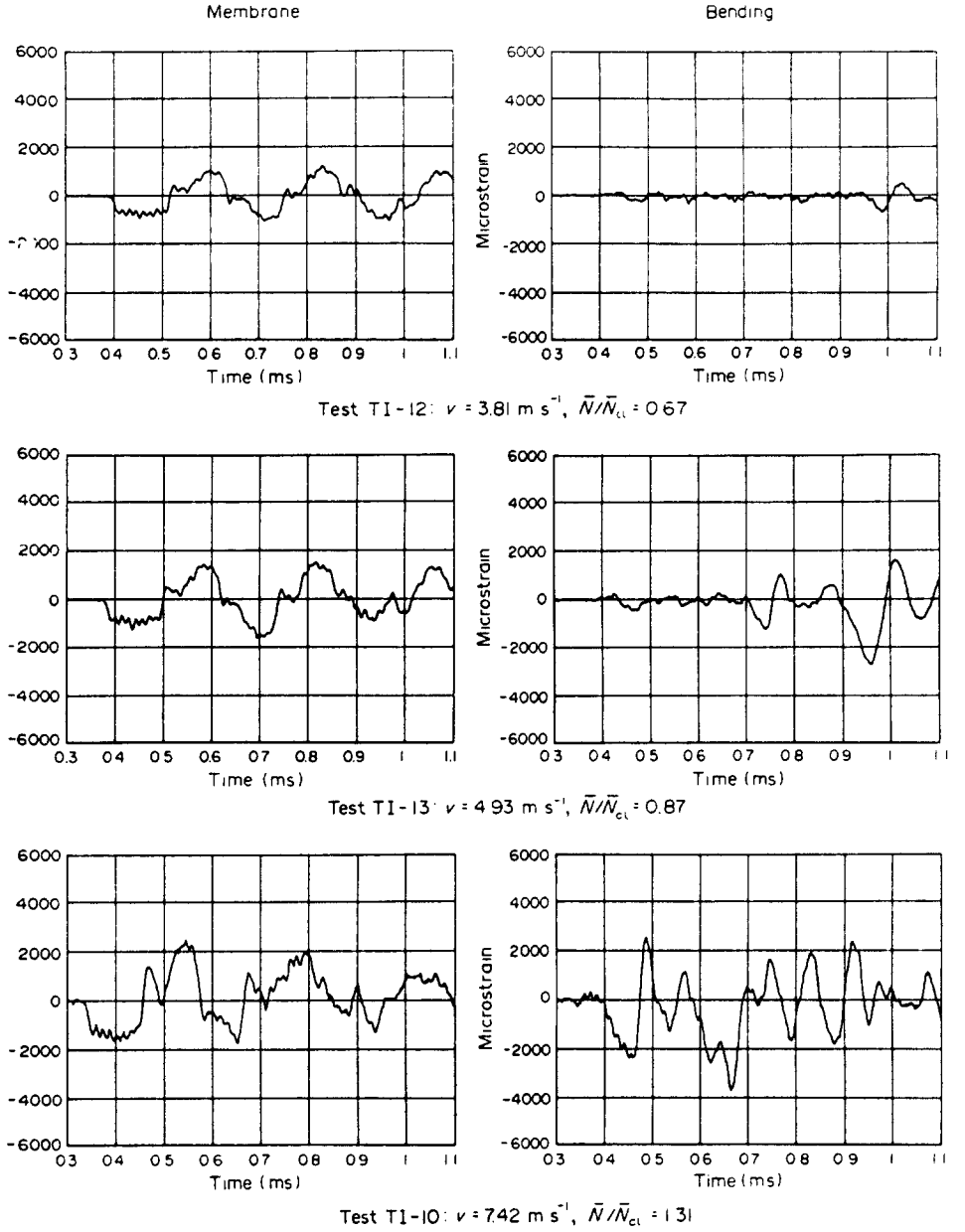

Fig. 12. Axial membrane and bending strains at $x = 15.2$ mm for three increasing impact velocities—experimental results.

4.3. *Higher impact load*

Figure 11 gives high-speed photographs of a shell impacted at a still higher velocity such that $\bar{N}/\bar{N}_{cl} = 2.19$. These photographs show even more clearly that initial buckling is dominated by symmetric buckles, because the axial bending is so severe that the light source images were reflected out of the field of view of the camera objective lens except for locations near outward crests of the buckles. As a result, the originally continuous reflected image lines become broken up by the buckling and the axial buckle wavelengths are apparent (e.g. in the photograph for $t = 0.435$ ms). At later times the line images become grossly distorted, as in Fig. 9, but again, all of this buckling was elastic. The only permanent deformation was a single, symmetric buckle at the base of the shell.

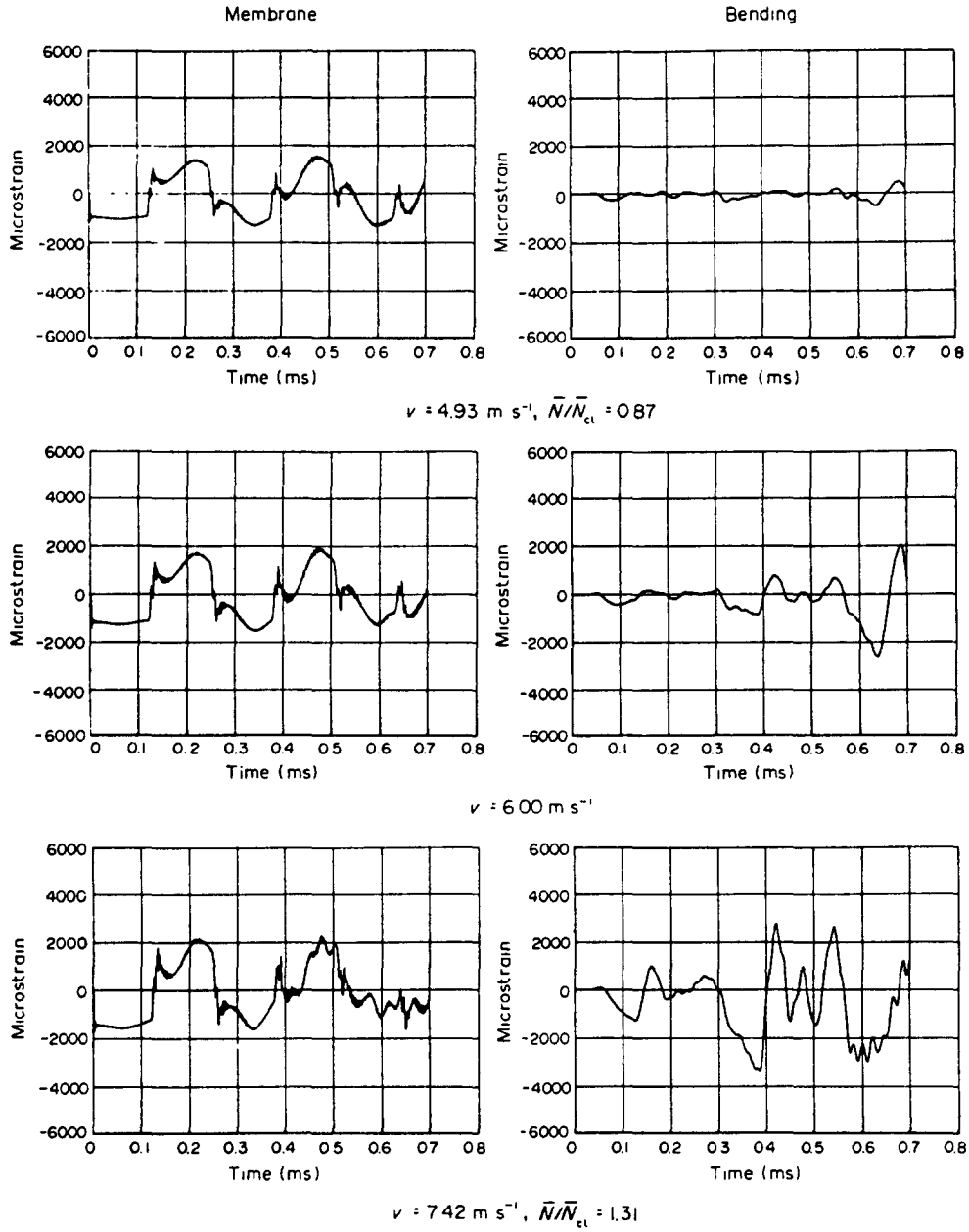

Fig. 13. Axial membrane and bending strains at $x = 15.2$ mm for three increasing impact velocities—theoretical results.

4.4. *Comparison of multipulse buckle strains*

Figures 12 and 13 summarize these results by comparing axial strain histories for sequences of three increasing impact velocities. For the experimental strains, in Fig. 12, the impact velocities give $\bar{N}/\bar{N}_{cl} = 0.67$, 0.87, and 1.31. At the lowest load, buckling has grown to a measurable amplitude near the end of the third axial compression. At the intermediate load, measurable buckling begins during the second compression and is substantially amplified during the third compression. At the highest velocity, buckling during the first compression is so severe that little further increase in buckle amplitude occurs during the second compression and the membrane strain energy is depleted so that there is no distinct third compression.

Essentially the same sequence is reproduced by the calculated strain histories in Fig. 13. In the calculations, the two lower velocities were increased so that the sequence of loads were $\bar{N}/\bar{N}_{cl} = 0.87$, 1.06, and 1.31. This was done because the neglect of asymmetric

buckling in these calculations makes the theory inappropriate for lower load levels (see the discussion at the end of the section on subclassical impact load). Inclusion of these modes would bring theory and experiment into even closer agreement, as suggested by the simple single-pulse theory with finite $\bar{N}_\theta$ discussed in Section 2.

5. SUMMARY AND CONCLUSIONS

Careful experiments compared with straightforward calculations of dynamic buckling in cylindrical shells under multipulse axial loading have shown that the essential features of the buckling are reproduced by the theory. For pulses comparable in duration to the hoop breathing mode of shell response, circumferential resultant forces and symmetric breathing deformations play a significant role in the response. Over a range of pulse amplitudes lower than the classical static axial buckling load, the circumferential force induces a broad group of asymmetric modes to grow exponentially with time. Thus, there is a continuous range of axial impact loads extending to values below the static buckling load for which dynamic buckling occurs within the scope of classical buckling theory. For impact loads higher than the classical static buckling load, the breathing deformations provide a deterministic mechanism that initiates symmetric buckling which dominates response during the initial compression pulse.

As in single-pulse buckling, another essential conclusion is that dynamic buckling under finite duration loadings is fundamentally a response phenomenon, and that the criterion for critical loads is one of allowable growth. For multiple pulses in thin-walled shells, an important feature of this growth is that the region of buckling spreads over the shell during the intervals between compression pulses. As a result, the integrated impulse of the compressive pulses can be substantially larger than the critical impulse for a single pulse because of the resulting increased energy absorbing capacity of the shell within an allowable stress or deformation.

Acknowledgements—This work was performed at SRI International with sponsorship by the Defense Nuclear Agency under contract DNA 001-81-C-0031. The DNA technical monitors were Lt. Col. E. Case and Lt. Cmdr. T. Butler. The authors would also like to thank D. Ploeger, who designed an early version of the impact loading machine, and the technical staff of the Poulter Laboratory at SRI, who performed the experiments and reduced the strain and photographic data.

REFERENCES

1. A. P. Coppa and W. A. Nash, Dynamic buckling of shell structures subject to longitudinal impact, Report to Air Force Flight Dyn. Lab., Dayton, Ohio, from General Electric Co., Philadelphia, PA 19101, FDL-TDR-64-65 (1964).
2. B. O. Almroth, A. M. C. Holmes and D. O. Brush, An experimental study of the buckling of cylinders under axial compression. *Expl. Mech.* **4**, 263–270 (1964).
3. R. S. Roth and J. M. Klosner, Nonlinear response of cylindrical shells with imperfections subjected to dynamic axial loads. *AIAA J.* **2**, 1788–1794 (1964).
4. J. W. Hutchinson and B. Budiansky, Dynamic buckling estimates. *AIAA J.* **4**, 525–530 (1966).
5. H. E. Lindberg and R. E. Herbert, Dynamic buckling of a thin cylindrical shell under axial impact. *ASME Trans.* **88**, *Series E, J. Appl. Mech.* **33**, 105–112 (1966).
6. H. Schwieger and C. Spudia, Investigation of the dynamic stability of axially impacted cylindrical shells (in German), Deutsche Luft- und Raumfahrt, Rep. DLR FB 70-19, Mulheim (Ruhr), West Germany (1970).
7. V. M. Kornev and V. N. Solodovnikov, Axially symmetrical instability modes in a cylindrical shell under impact. *Z. Prikl. Mek. Tek. Fiz.* 95–100 (1972).
8. Y. S. Tamura and C. D. Babcock, Dynamic stability of cylindrical shells under step loading. *ASME Trans.* **97**, *Series E, J. Appl. Mech.* **42**, 190–194 (1975).
9. G. Maymon and A. Libai, Dynamics and failure of cylindrical shells subjected to axial impact. *AIAA J.* **15**, 1624–1630 (1977).
10. D. G. Zimcik and R. C. Tennyson, Stability of circular cylindrical shells under transient axial impulsive loading. *AIAA J.* **18**, 691–699 (1980).
11. T. Belytschko and R. Mullen, WHAMS: a program for transient analysis of structures and continua. In *Structural Mechanics Software Series* (Edited by N. Perrone *et al.*), Vol. 2, pp. 151–212 (1978).
12. H. E. Lindberg and A. L. Florence, *Dynamic Pulse Buckling, Theory and Experiment*, DNA 6503H. Defense Nuclear Agency Press, Washington, DC (1983).